In vivo Assembly of Bacterial Partition Condensates on Supercoiled and Linear DNA

Hicham Sekkouri Alaoui[1], Valentin Quèbre[1], Linda Delimi[2], Jérôme Rech[1], Debaugny-Diaz Roxanne[1], Delphine Labourdette[3], Manuel Campos[1], François Cornet[1], Jean-Charles Walter[2] and Jean-Yves Bouet[1]*

[1] Laboratoire de Microbiologie et Génétique Moléculaires, Centre de Biologie Intégrative (CBI), Centre National de la Recherche Scientifique (CNRS), Université de Toulouse Paul Sabatier, UPS, F-31062 Toulouse, France.

[2] Laboratoire Charles Coulomb (L2C), Université de Montpellier, CNRS, Montpellier, France.

[3] TBI, Université de Toulouse, CNRS, INRA, INSA, Toulouse, France.

*Correspondence should be addressed to jean-yves.bouet@univ-tlse3.fr

Summary

In bacteria, faithful DNA segregation of chromosomes and plasmids is mainly mediated by ParABS systems. These systems, consisting of the ParA ATPase, the DNA binding ParB CTPase, and the centromere site *parS*, orchestrate the separation of newly replicated DNA copies and their positioning along the cell's longitudinal axis. Accurate segregation relies on the assembly of a high-molecular-weight complex made of hundreds of ParB dimers assembled from *parS* nucleation sites. This complex assembles in a multi-step process and exhibits dynamic liquid-droplet properties. Despite various proposed models, including 'Nucleation & caging' and 'Clamping & sliding', the complete mechanism for partition complex assembly remains elusive. This study, focusing on the plasmid F, investigates the impact of DNA supercoiling on ParB DNA binding profiles *in vivo*. We found that variation in DNA supercoiling does not significantly affect any step of the assembly of the partition complex. Physical modeling, based on ChIP-seq data from linear plasmids F, challenges the sufficiency of the 'Clamping & sliding' model alone. It demonstrates that while this model fits ParB DNA binding profiles up to ~2-kbp from *parS*, additional mechanisms like 'Nucleation & caging' are needed for distant ParB binding. The study also highlights the dominant role of ParB-ParB interactions in DNA compaction within ParB condensates.

Keywords (up to six keywords)

DNA supercoiling, Linear DNA, Partition complex, ParB condensate, Bridging, Plasmids

Introduction

In bacteria, faithful DNA segregation is essential and ensures that cell offsprings receive at least one copy of each replicon, chromosome or plasmids, after their replication. This process involves the separation and transportation of the new copies in opposite directions along the cell's longitudinal axis (Cornet et al., 2023). The partitioning of chromosomes and most low-copy number plasmids relies on ParABS systems, which consist of ParA, a Walker-type ATPase, and ParB, a site-specific DNA binding protein and CTPase (Bouet and Funnell, 2019; Jalal and Le, 2020). ParB binds to a few centromeric sites, termed *parS*, and further assembles in a large nucleoprotein complex, called the partition complex. ParA action separates the partition complexes, through the stimulation of its ATPase activity by ParB (Ah-Seng et al., 2013), and actively relocates them in opposite directions. The *parS* sites, present in 1-10 copies located near the origins of replication, allow the positioning of the Ori domain rapidly after replication by reaching particular positions. Depending on the bacterial species and replicons, these positions are either at quarter-cell positions (*e.g.*, P1 and F plasmids (Gordon et al., 1997; Niki and Hiraga, 1997)), the edges of the nucleoid (*e.g.*, *M. xanthus* (Harms et al., 2013)) or at the cell poles (*e.g.*, *C. crescentus* (Bowman et al., 2008)), all ensuring an accurate segregation of Ori domains.

Partition complexes are high molecular weight structures. Their assemblies are initiated by a sequential multi-step process (Figure 1): (i) the specific binding of ParB to *parS*, usually a 16-bp DNA motif (Lin and Grossman, 1998; Livny et al., 2007; Pillet et al., 2011), (ii) the binding of CTP to *parS*-bound ParB (Osorio-Valeriano et al., 2019; Soh et al., 2019), followed by (iii) the conversion of ParB into a clamp over *parS* and its ejection from *parS* due to a steric clash upon ParB remodeling (Jalal et al., 2020), (iv) the subsequent sliding over *parS*-proximal DNA (Soh et al., 2019), and lastly (v) the ParB unloading after clamp opening. Interestingly, it has also been shown that partition complexes are dynamic structures that display some properties of a liquid-droplet, *i.e.*, an assembly that may be mediated by phase separation (Azaldegui et al., 2020). These properties include (i) the rapid exchange of ParB between separate partition complexes in the order of a few minutes (Debaugny et al., 2018; Osorio-Valeriano et al., 2021), (ii) the intracellular mobility of ParB is ~100 times slower inside ParB clusters (concentrated phase) than outside (diluted phase) (Guilhas et al., 2020), (iii) the ability of ParB foci to fuse when ParA is degradated (Guilhas et al., 2020), and (iv) the self-organization of ParB into droplets *in vitro* (Babl et al., 2022). Which mechanisms are at play to assemble these high molecular weight structures, essential for DNA segregation, is not yet fully understood.

Several models have been suggested to explain the assembly of the partition complex, including the most recent ones, namely 'Nucleation & caging' (N&C) and 'Clamping & sliding' (C&S) (Jalal and Le, 2020). This latter was proposed based on the finding that ParB is a CTPase that clamps over *parS* DNA and subsequently diffuses along the DNA until the clamp opens (Figure 1B). The physical modeling of ParB DNA profiles through an exponential decay of ParB binding probability along the *parS*-proximal DNA could depict the 'C&S' on naked DNA (Osorio-Valeriano et al., 2021; Walter et al., 2020). However, this model did not align with some biochemical characteristics of ParB, especially the rates of release from *parS* and of unloading from the DNA (Walter et al., 2020). Additionally, it failed to explain (i) the fast reloading of the partition complex post DNA replication and (ii) the presence of numerous proteins that are bound all along the DNA expected to impede ParB diffusion (Walter et al., 2020). Conversely, 'N&C' describe a power-law decay of the probability of ParB binding along the *parS*-proximal DNA which was proposed to account for the attraction of most ParB dimers to a few ParB nucleated from *parS* sites by the combination of low but synergistic interactions, namely ParB-ParB and ParB-non-specific DNA (Debaugny et al., 2018; Sanchez et al., 2015). This stochastic binding model, however, was proposed before the finding that ParB forms CTP-dependent clamps. A combination between these two models has thus been proposed to describe the ParB DNA binding profile with 'C&S' and 'N&C' primarily acting at short and long distances from *parS*, respectively (Walter et al., 2020).

The modeling of 'Nucleation & caging' suggests that DNA compaction plays a role in the structure of the ParBS complexes DNA compaction (Sanchez et al., 2015). In living system, DNA compaction predominantly arise from DNA supercoiling (Junier et al., 2023) and/or DNA bridging (van der Valk et al., 2014). In this study, we explored the impact of the variation of DNA supercoiling on the ParB DNA binding profile *in vivo*. Our findings indicate that the assembly of the partition complex of the plasmid F is largely insensitive to significant variations in DNA supercoiling. In addition, using linear plasmid DNA, we also observed an unaltered ParB DNA binding profile compared to supercoiled DNA. Using physical modeling from the ChIP-seq data obtained on a linear plasmid F with DNA ends in the ParB spreading zone, we further demonstrated that the 'C&S' alone cannot account for the assembly of the partition complex. Altogether, these data therefore comfort a model of partition complex assembly with two mechanisms at play, and with DNA compaction primarily arising from ParB-mediated DNA bridging.

Results

ParB DNA binding pattern is invariant to DNA supercoiling variations

To investigate whether one or several steps of the assembly of the partition complex is sensitive to DNA supercoiling, we assayed the DNA binding profile of ParB from the plasmid F *in vivo*. This profile, well described by high-resolution ChIP-sequencing (Debaugny et al., 2018; Sanchez et al., 2015), allows to detect ParB binding to *parS* sites, its release from *parS* upon CTP binding as a clamp over DNA as well as the ParB binding at long distance from *parS* (see Figure 1). The plasmid F (F1-10B; Debaugny et al., 2018) was conjugated in two natural hosts, *Escherichia coli* and *Salmonella typhimurium* LT2, that display ~15 % difference in supercoiling density (σ) (Champion and Higgins, 2007). F1-10B was also introduced in *E. coli topA* and LT2 *gyrB*652, deficient in topoisomerase I and Gyrase activities and harboring a higher and lower negative supercoiling level compare to WT, respectively (Champion and Higgins, 2007; Conter et al., 1997; Rovinskiy et al., 2019). F1-10B replicates and segregates faithfully in all these strains.

We first measured the relative supercoiling density between these four strains by introducing pSAH01, a small, medium copy-number plasmid (3.4-kbp). pSAH01 was extracted from exponentially growing cell cultures for *E. coli* at 37°C or LT2 at 30°C. Lowering the temperature reduces the negative supercoiling density (Goldstein and Drlica, 1984) which enables to extend the range of supercoiling to be tested. In addition, the LT2 *gyrB* allele is thermosensitive at 37°C. The relative topoisomers distributions were measured on agarose gels containing chloroquine followed by densitometric analyses (Figures 2A and S1A). As expected, pSAH01 is more negatively supercoiled in *E. coli topA* compare to WT with a difference of ~2.2 topoisomers in average. Comparing pSAH01 from *E. coli* to LT2, we found a relative difference of 1.1 topoisomers, in agreement with previous results (Champion and Higgins, 2007). Lastly, pSAH01 extracted from LT2 and LT2 *gyrB652* displays a variation of ~4.4 topoisomers, as quantified from 2D-gel analyses (Figure 2B).

To estimate the global supercoiling density in each strain, we then measured the variation of topoisomers distribution of pSAH01 between the least negatively supercoiled one obtained from LT2 *gyrB*652 by 2D gels and the relaxed form (Figures 2C and S1B-C). To note, for an easiest counting of the variation in topoisomers distribution, these two DNA preparations were mixed together (see legends). We found a difference between the two samples of 16.9 topoisomers in average. From the formula $\Delta\sigma = \Delta Lk / Lk_0$ with $Lk_0 = 323.3$ for pSAH01, we calculated an average supercoiling density in LT2 *gyrB652* of -0.052 (Figure 2D). The

supercoiling densities in each strain were then estimated using the relative σ variation between them. We found an average of -0.066, -0.069 and -0.076 for LT2 WT, *E. coli* WT and *E. coli topA*, respectively (Figure 2D). Overall, it represents a σ variation of 32% between the two extreme conditions. Considering that, *in vivo*, half of the supercoiling is titrated by proteins bound to DNA (Pettijohn and Pfenninger, 1980), the free supercoiling densities in these strains range from ~ -0.038 and -0.026.

To test whether DNA supercoiling has an impact on the ParB DNA binding profile, we performed ChIP-sequencing assays on the two strains with the greatest σ variation, *E. coli topA* and LT2 *gyrB*; the former displaying ~50 % more free supercoiled DNA density than the latter. The overall $ParB_F$ DNA binding profiles were highly reproducible between the two independent duplicates with $ParB_F$ binding found only on the F plasmid DNA but not on the *E. coli* chromosome, similarly to previous results in another lineage of *E. coli* (Figure S2A-B) (Debaugny et al., 2018; Sanchez et al., 2015). Strikingly, the profiles from the *topA* and *gyrB*652 strains around the $parS_F$ site are almost superimposable (Figure 3A). Moreover, the deeps and peaks in the signal on the right side of *parS* are essentially positioned at the same locations, which is corroborated by a high correlation coefficient (0.988). These data reveals that large intracellular variations of the DNA supercoiling level has no detectable effect on the $ParB_F$ DNA binding pattern in the wide range of σ tested. This data thus indicates that none of the steps in the assembly of the partition complex is sensitive to the DNA supercoiling level.

ParB DNA binding patterns on linear DNA molecules

To explore further the sensitivity of the partition complex assembly relative to DNA supercoiling, we investigated the $ParB_F$ DNA binding profile on linearized plasmid F DNA *in vivo*. We employed the capability of the coliphage N15 to be maintained as a prophage in a linear plasmid form through the action of the telomerase, TelN, on the *telRL* sites (Ravin, 2003). The clivage of *telRL* followed by 5'-3' joining and TelN releasing generates covalently closed hairpin structures at both extremities that are thus protected from exonuclease activities (Ravin, 2003). This strategy was previously shown to efficiently linearize the *E. coli* chromosome after insertion of *telRL* site in the terminus region (Cui et al., 2007). We constructed derivatives of the F1-10B by inserting *telRL* at three positions relative to the *parS* site (3.5-, 13- and 47-kbp from the last repeat of the 16-bp binding motif). These F_*telRL* plasmids are circular in the absence of TelN (Figure 4A and S3A-B). When conjugated in a

strain carrying the N15 prophage, the F_*telRL* plasmids are efficiently converted to linear DNA molecules as confirmed by a PCR-based assay (Figure S3A-C).

To control that partition complexes are able to assemble on linear plasmids, we imaged F-*telRL* plasmids, expressing the ParB-mVenus fusion at its endogenous position, by fluorescence microscopy (Figure 4B). We found that, for the three insertion positions, ParB foci are bright with low intracellular background in both the absence and presence of N15. This indicates that partition complexes assemble correctly on the linear F-plasmids. We noticed, however, that in the presence of N15 some cells from the strain carrying F_*telRL*3.5 do not harbor foci suggesting a default in plasmid maintenance, either replication or partition. We confirmed this default by performing a plasmid stability assay (Figure 4C). While the linear F_*telRL*47 and F_*telRL*13 are as stable as the circular F1-10B plasmid (loss rates < 0.02 %), the F_*telRL*3.5 is lost at ~0.5% per cell per generation. This later loss rate, in agreement with the microcopy observation, is however well below random segregation. Indeed, in this growth condition, a circular plasmid F deleted from *parAB* is lost at ~3%. To discriminate whether this maintenance deficiency arises from a default in the replication or the partition process, we quantified the intracellular positioning of the F plasmids derivatives, which is dependent on a functional ParABS system. Indeed, ParB foci are colocalized with the F-plasmid around mid- or quarter-cell positions in cells with one or two foci, respectively, or are equi-positioned in cells with >2 foci (Diaz et al., 2015). We found that the positions of the three F-*telRL* plasmids, in the circular (-N15) or linear (+N15) forms, are localized around mid-cell (1 focus cells) or quarter positions (two foci cells) similarly to F1-10B (Figure 4D). This result thus indicates that the positioning pattern, and thus partition, is unaffected in the linear forms. The slight loss deficiency observed for F-*telRL*3.5 in the linear form is therefore most likely due to a replication default. All together, these data indicate that the three linear F plasmids are faithfully segregated, and thus that functional partition complexes are assembled on their *parS* centromere sites independently of the position of the telomerization site.

The assembly of the partition complex on linear F plasmids was further deciphered by investigating the $ParB_F$ DNA pattern by ChIP-sequencing as above. For linear F_*telRL*47 and *F_telRL*13, in which the telomerisation sites are located outside of the ParB DNA binding zone, the overall profiles were highly similar with high enrichment at and in the close vicinity of *parS* (Fig. S4A-B). Notably, when normalize relatively to the maximum reads, these ParB DNA binding profiles are also very similar to the ones obtained from the circular F1-10B (Figure S5A-B), except for the absence of signal at the *telRL* insertion sites as expected (insets). In these two cases, no change is observed in (i) the initial drop after *parS* sites, (ii)

the relative ParB density over the extend of ParB DNA binding zone and (iii) the pattern of deep and peaks. These data indicate that the linearization of the plasmid F does not change the specific binding to *parS*, its ejection upon CTP binding and its long range binding over *parS*-proximal DNA, even when a DNA extremity is at a few Kbp of the ParB binding zone. This thus confirms that the overall assembly of the partition complex is independent of the level of DNA supercoiling.

Partition complex assembly with linearization within the ParB DNA binding zone

We investigated the partition complex assembly on the plasmid F linearized at ~3.5 Kpb of *parS*, *i.e.*, with an extremity positioned in the first part of the ParB DNA binding zone. This is readily observed on the ChIP-seq profiles with an abrupt drop of the number of reads just before the *telRL* site (Figures S4C and S5C). Strikingly, the relative ParB DNA binding profile of the F_*telRL*3.5 between *parS* and the telomerization site was very similar to the ones of the circular F1-10B and the linear F_*telRL13* and F_*telRL47*, only differing in the last ~400-bp before the telomerization site (Figure 5A). Given the size of the ChIP-seq libraries (~175-bp; see Table S2), the very low ParB density within the ~200-bp proximal to the *telRL* site was expected (Debaugny et al., 2018). The remaining ~200-bp, which corresponds to the observed signal drop, likely indicates the release of ParB from the free DNA end as sliding clamps.

In all cases tested, the relative ParB levels are thus superimposable from *parS* to the drop close the DNA ends (Figure 5A). Moreover, the deep and peaks are at the same locations. This clearly indicates that (i) the ParB binding to *parS*, (ii) the CTP-dependent ejection of ParB from *parS* and (iii) the subsequent steps including sliding are unchanged between linear and supercoiled DNA.

ParB clamps diffuse from *parS* over ~2-kbp

The ParB DNA binding profile obtained from the linear plasmid F linearized at 3.5-Kbp from *parS* provide a valuable data set for assessing whether it can be exclusively described by the 'Clamping & sliding' model (Figure 1B). Briefly, the physico-mathematical modeling of this mechanism is based on the equation for the evolution of the unidimensional density described in Experimental procedures (fully described in Walter et al., 2020). In the case of the linear plasmid with DNA ends, ParB clamps escape from the DNA without the possibility of re-entering from the extremity. Consequently, the DNA ends acts as a sink for ParB clamps. Monte Carlo simulations were conducted based on this modeling applied to a linear DNA

with an extremity (*i.e.*, an absorbing boundary condition (BC) in physical terms) positioned at 3.5-kpb from *parS* for two sets of parameters.

Firstly, we employed the previously fitted parameters (see experimental procedures), including the release kinetics R = 1.9 s^{-1} (Walter et al., 2020). The 'C&S' modeling with absorbing BC, as opposed to the periodic BC used for circular plasmid, displays a continuous decrease in ParB density from *parS* to the absorbing boundary where $n(x) = 0$ (Figure 5B). The boundary effect leads to a profile that decreases more rapidly than the periodic BC case (Walter et al., 2020). The ParB DNA binding profile of the linear plasmid F_*telRL*3.5 clearly disagrees with the model's prediction. Indeed, the former shows an identical profile as the circular WT case up to ~400-bp from the extremity, after which the profile drops to zero.

Secondly, since the overall density of the theoretical profile is diminished compared to previous modeling (Walter et al., 2020) due to the escape of ParB at the telomere, we tested an increased release parameter (R = 3 s^{-1}) to align with the experimental data. This adjustment reasonably describes the first half of the ParB density profile but fail to depict accurately the second half. Thus, even with an adjusted release parameter (R = 3 s^{-1}), the model fits well over a span of ~2-Kpb, but fails between 2-kbp and the DNA end. This modeling strongly indicates that the 'Clamping & sliding' mechanism alone cannot entirely explain the ParB binding profile on a DNA with *parS* located at 3.5 kbp from the DNA end. Another mechanism is therefore needed to account for the ParB binding profile after 2-kbp.

ParB-ParB interactions dominate supercoiling in DNA compaction within ParB condensates

The invariance of the ChIP-seq ParB profiles following linearization suggests that, within the framework of the 'N&C' model (for details, see Fig. S6), the average radius of gyration *R_g* of the plasmids is mainly unchanged upon the release of supercoiling. The 'N&C' model posits that the primary determinant shaping the ParB profile is the averaged distance of DNA from *parS*, *i.e.*, the radius of gyration (Fig. S6A). Supercoiling has been observed to induce DNA compaction of approximately 30% (Walter et al., 2021). Based on recent experimental studies (*e.g.*, Balaguer et al., 2021; Tisma et al., 2023) and previous work (*e.g.*, Sanchez et al., 2015; Surtees and Funnell, 1999), we investigated the contribution of *in trans* ParB-ParB interactions to DNA compaction within the ParB enrichment zone.

We performed Monte Carlo simulations (Newman and Barkema, 1999) of a polymer containing interacting particles representing ParB, as depicted in Fig. 6A (for details, see Fig. S6A). We coarse-grained an open plasmid of 13-Kbp (corresponding to the ParB enriched

region) at the experimental resolution scale, *i.e.*, 20-bp (the footprint of ParB binding (Sanchez et al., 2015)), yielding a self-avoiding walk polymer (Vanderzande, 1998) of length N=658 monomers embedded into a face centered cubic (FCC) lattice. Initially, *Nb* ~70 ParB proteins were distributed on the polymer according to the ChIP-seq distribution profile. Subsequently, the polymer was allowed to move, and after thermalization at the coupling energy J, the radius of gyration was sampled. This process was repeated for 600 realizations of independent initial ParB distributions. The simulations were carried out with increasing values of the attractive energy *J* between ParB proteins, which interact when two are close in space but distant along DNA (Fig. 6A). The root mean squared radius of gyration plotted against a range of energy *J* shows that the polymer becomes more compact as *J* increases (Fig. 6B). Polymers are in coiled conformations when J < 1 and in globular conformations when $J > 3$. We estimated a critical value J_c ~1.70 +/- 0.1 kT (for details, see Fig. S7). The level of compaction was computed using the formula $(R_{coil}-R_{glob}) / R_{coil}$, where R_{coil} *and* R_{glob} represent the radius of gyration in the coil and the globule phases, respectively. We observed a reduction in the radius of gyration by a factor of 40% induced by ParB-ParB interactions. Importantly, in all cases, the degree of compaction of ~40% surpasses the ~30% effect observed with supercoiling (Walter et al., 2021). These modeling data thus corroborate the minimal impact of the variation of DNA supercoiling on DNA compaction within ParB condensates, supporting the notion that this compaction primarily arises from ParB-ParB interactions in a supercoiling independent manner.

Discussion

In this work, we tested experimentally the role of DNA supercoiling in the assembly of the ParB condensate. We employed the conjugative 100-kbp F-plasmid since it allows to test different levels of supercoiling in non-isogenic strains, and to design large linear plasmids that are propagating in growing bacterial population. These properties permitted us to test the $ParB_F$ DNA binding profiles over a wide range of supercoiling levels and to demonstrate that DNA supercoiling has little impact, if any, on the multi-step assembly of the partition complex. Furthermore, alongside with the ChIP-sequencing data of $ParB_F$, the physico-mathematical modeling of the DNA binding profiles provides new evidence for a coupled mechanism for explaining ParB binding at long distances from *parS*. It also supports that ParB-ParB bridging interactions, rather than DNA supercoiling, are the primary determinant for DNA compaction in the ParB condensates.

Mutations affecting DNA topology have long been known to induce deficiencies in mini-F plasmid partitioning. In the case of *E. coli gyrB* mutants, such impairment was initially attributed to plasmid relaxation and/or overexpression of $ParB_F$, affecting its interaction with *parS* (Ogura et al., 1990). Despite this phenotype, referred to as IncG incompatibility, has since been elucidated as a consequence of the $ParB_F$-induced formation of mini-F multimers in the absence of the ResD/*rfsF* dimer resolution system (Bouet et al., 2006), the question of whether DNA supercoiling influences the assembly of the partition complex remained open. Recent physical modeling, based on ChIP-sequencing data, suggested that DNA compaction needed for the 'N&C' based-modeling might be predominantly attributed to DNA supercoiling within the physiological range (Walter et al., 2021). We have investigated this possibility by measuring the ParB DNA binding profiles in two natural hosts of the plasmid F mutated for topoisomerase activities, *E. coli topA* and LT2 *gyrB*, exhibiting extreme DNA supercoiling levels (Figure 2). We also investigated F-plasmids propagating as linear DNA molecules and proved to be unaffected in the partitioning process (Figures 4 and S3). We found that the ParB DNA binding profiles are highly similar across all conditions, resembling those obtained from the circular plasmid F at wt level of total DNA supercoiling. In particular, the release of clamped ParB from *parS*, observed by the rapid decrease of ParB density after *parS* followed by slow decaying over 0.2- to 2-kbp, is almost superimposable in all conditions tested (Figures 3 and 5). The long distance (2- to 12-kbp from *parS*) decays of the ParB density are also similar. Our data thus indicates that none of the steps involved in the auto-assembly of ParB condensates are sensitive to DNA supercoiling level and to the structural form of the DNA molecule, whether circular or linear.

The assembly of partition complex on mini-F plasmids triggers a strong deficit in their negative supercoiling level by 10-12 superhelical turns (Biek and Shi, 1994). This deficit, specifically dependent on $ParB_F$ and $parS_F$, was proposed to arise from interference with the action of the DNA gyrase on the mini-F plasmids (Bouet and Lane, 2009), similarly to the ParB silencing that prevents RNA polymerase to access promoters in proximity of *parS* (Rodionov et al., 1999). The high local concentration of ParB in the vicinity of *parS*, exceeding 5 mM (Guilhas et al., 2020), would be sufficient to impede the access of DNA gyrase to the mini-F DNA. Indeed, mini-F plasmids are typically between 7- and 12-kpb in size, a DNA length that might be entirely trapped within the ParB condensate. In contrast, for naturally occurring F plasmids (70- to 200-kbp), the ParB DNA binding zone represents less than 20 % of the plasmid size thus allowing the access of DNA gyrase at long distance from *parS*. The regulation of the homeostasis of DNA supercoiling on such large plasmids should

be fully effective given the diffuse nature of supercoils (Junier et al., 2023 and refs therein). One could thus expected that ParB-induced deficit in negative supercoils may not occur, or is strongly reduced, on large, naturally occurring plasmids. This, however, remains to be experimentally determined.

The predominant fraction of intracellular ParB dimers (> 90%) forms densely packed clusters assembled at *parS* sites (Sanchez et al., 2015). These ParB condensates exhibit dynamic characteristics, with a high exchange of ParB rate between condensates (Debaugny et al., 2018; Osorio-Valeriano et al., 2021; Tisma et al., 2023). Upon binding to *parS* and CTP, ParB dimers undergo an important conformational change, transitioning from *parS* binding to clamping onto flanking DNA (see Figure 1B). Clamped-ParB can diffuse over long distance along naked DNA *in vitro* (Soh et al., 2019). These properties were initially considered to be sufficient to explain the ParB DNA binding profiles (Osorio-Valeriano et al., 2021). However, attempts to model these profiles using a 'Clamping & sliding' mechanism, based on experimentally determined parameters, failed to explain ChIP-seq data, possibly due to constraints imposed by numerous roadblocks formed by DNA-bound proteins (Walter et al., 2020).

In this study, we provided further evidence *in vivo* that the 'Clamping & sliding' model alone is not sufficient to explain the ParB DNA binding profile. We took advantage of the linear plasmid F with a telomere site at 3.5-kbp of *parS*. It displays an unaltered ParB DNA binding profile (Figure 5B), in strike contradiction with the pattern expected from the model 'Clamping & sliding' which predicts a gradual ParB density decay up to the DNA end, acting as a sink for ParB clamps. The ParB density only changes abruptly in the last ~400-bp where ParB can efficiently escape through the DNA end by rapid diffusion. Interestingly, however, the 'Clamping & sliding' model adequately describes the progressive decay of ParB density up to ~2-kbp, suggesting that it can account for the ParB DNA binding profiles only up to a short distance from *parS*. This observation clearly supports the proposal that, in addition to ParB diffusion along the DNA, another mechanism is at play to explain the ParB DNA binding profiles at larger distance from *parS*.

The model 'Nucleation & caging' proposed that long-distance ParB-ParB interactions are crucial for condensate formation around *parS* (Sanchez et al., 2015). Recent *in vitro* observations have revealed that ParB can also be loaded independently from *parS* through interaction with a clamped ParB, enabling some ParB to be clamped and diffuse on any DNA present in the spatial proximity to *parS*. This offers the possibility to bypass protein roadblocks and to bridge transiently distant DNA (Tisma et al., 2022). This phenomenon was

accounted for in the 'Nucleation & caging' model as part of the stochastic ParB-ParB interactions which also comprises other ParB-ParB interactions, *in cis* and *in trans* of *parS*, not necessarily involving ParB clamps, as observed experimentally (Sanchez et al., 2015; Tisma et al., 2023). In all cases, the combination of all these interactions increases the valence of ParB needed to cluster efficiently most ParB around *parS* and to compact DNA.

The bridging interactions mediated by ParB and CTP have been shown *in vitro* to induce significant compaction specifically on DNA carrying *parS* sequences (Balaguer et al., 2021; Tisma et al., 2023). By employing physical modeling of ParB DNA binding profiles, we assessed the relative contributions of DNA supercoiling and ParB bridging interactions to DNA compaction within ParB condensates. Within the 'Nucleation & caging' framework, DNA supercoiling was estimated to yield a threefold compaction effect *in vivo* (Walter et al., 2021). Employing the same modeling framework, we found that ParB-ParB interactions contribute to DNA compaction by approximately ~40% (Fig. 6B), slightly exceeding the ~30% attributed to DNA supercoiling. The consistent robustness of the ParB DNA binding profiles in all tested conditions indicates that ParB-ParB interactions acts independently, but not additionally, to DNA supercoiling. Consequently, our results highlight the primary role of the ParB-ParB interactions as the main driver of DNA compaction in ParB condensates. Notably, this mechanism imparts independence to the ParABS system from host factors and enables resilience to various growth conditions. Specifically, for plasmids capable of efficient inter-strain transfer, this independence enables the autonomous assembly of partition condensates independently of the host cells, facilitating adaptation to rapid changes in growth conditions such as environmental stresses affecting DNA supercoiling. Moreover, the presence of highly conserved ParABS systems not only on circular DNA molecules but also on linear plasmids or prophages such as K02, PY54, and N15, as well as on linear chromosomes in bacteria such as Streptomyces and Borrelia, underscores their adaptability to diverse genetic contexts.

Lastly, it is noteworthy to emphasize that ParB-mediated partition condensates from various plasmid systems serve as thorough and complementary models for understanding bacterial DNA partitioning. Indeed, ParB encoded by plasmids, such as F or RK2, exhibit highly conserved features shared with their chromosomal counterparts. Notably, the binding to dedicated 16-bp *parS* sites and the presence of a ParB DNA binding domain, unusually composed of two distinct centromere binding motifs, called CBM1 and CBM2 (Sanchez et al., 2013). The remarkable conservation of these characteristics may stem from mechanistic constraints, particularly the ejection of ParB clamps arising from the steric hindrance by the

CBM2 motif after the CTP-induced remodeling (Jalal et al., 2021). Altogether, the mechanisms involved in the assembly of ParB condensates allow for a high level of robustness, which aligns well with the adaptability to nucleate on DNA molecules with varying level of DNA supercoiling, diverse structural shapes and different lengths, whether linear or circular and encompassing plasmids or chromosomes DNA molecules.

EXPERIMENTAL PROCEDURES

Bacterial strains, plasmids and oligonucleotides

Strains are derivatives of *E. coli* K12 or *Salmonella typhimurium* LT2 (called LT2 in the text) are listed, together with plasmids, in Table S1. LT2 strains NH2837 and NH2678 are gift from P. Higgins. Constructions of plasmids and strains are detailed in Supplementary materials. Oligonucleotides used in the study are listed in Table S3.

Topoisomers analyses

The strains carrying pSAH01 were grown overnight in LB medium, supplemented with ampicillin, under agitation at 37°C or 30°C for *E. coli* or LT2 strains, respectively. The cultures were diluted 200 times in the same medium, and cells were harvested at OD_{600} ~0.6 by centrifugation of 25 ml. After 2 washes in TE1X, pSAH01 was purified using the MIDI DNA purification kit (Qiagen) and kept à -20°C until use. Topoisomers distributions were analyzed by electrophoresis on 1% agarose gel in 40 mM Tris acetate, 1mMEDTA, as previously described (Bouet and Lane, 2009). Chloroquine concentrations, ranging from 0.5 to 8 $\mu g.ml^{-1}$ are indicated in the figure legends. Gels were stained with Sybr green before scanning.

Densitometric analyses were performed using Image J software. The relative variation of DNA supercoiling density ($\Delta\sigma$) of pSAH01 between two strains are estimated from the difference in the Gaussian distributions of topoisomers or linking number (ΔLK) divided by the linking number LK_0 of the plasmid (LK_0 = plasmid size / 10.5 = 323).

Relaxed CCC DNA was prepared by incubating pSAH01 with Topo I (Invitrogen) in the recommended buffer. Removal of supercoils was verified by agarose gel electrophoresis, and subsequently used in 2D-gel electrophoresis.

Chromatin immunoprecipitation DNA sequencing (ChIP-seq)

High resolution ChIP-sequencing was carried out using an affinity-purified anti-ParB antibody as previously described (Diaz et al., 2017) with the following modification.

Sonication was performed at 10°C using a Covaris® m220 focused ultrasonicator (200 cycles at 75 W for 350 seconds) on aliquots (120 µl), which were then pooled in LoBind tubes for subsequent steps.

The ChIP-seq data (each assays with relevant information are summarized in Table S2) were processed using RStudio software with custom scripts (available upon request). ParB reads were counted at the center of the DNA fragments, taking into account the average size of each DNA library. Background levels on the plasmid F were determined by averaging ParB reads within genomic positions ranging from 1- to 31-kbp and 74- to 99-kbp. Following background subtraction, a smoothing function was applied by averaging over a 40-bp window with a step size of 20-bp. ParB density was obtained by normalizing reads relative to the highest value.

For quantitative comparison between replicates, the number of reads were normalized relative to the number of mapped reads.

Correlation analyses were performed as previously (Debaugny et al., 2018) using the formula:

$$Correl(x, y) = \frac{\sum(x - \bar{x})(y - \bar{y})}{\sqrt{\sum(x - \bar{x})^2 \sum(y - \bar{y})^2}}$$

Epifluorescence microscopy

The strains expressing the fluorescent proteins were grown overnight at 30°C in M9-glucose-CSA medium. The cultures were diluted 250 times in the same medium and incubated at 30°C until OD_{600nm} ~0.3. 0.7 µl of culture were spotted onto slides coated with a 1% agarose buffered in M9 solution and images were acquired as previously described (Diaz et al., 2015). Nis-Elements AR software (Nikon) was used for image capture and editing. Image analysis was done using ImageJ softwares. The foci counting and positioning on the longitudinal cell axis, were carried out using the macro “Coli inspector” and the plugin “ObjectJ”.

Plasmid stability assay

The experiments and the calculation of the loss rate per generation were performed essentially as previously described (Sanchez et al., 2013).

Physical modeling of the 'Clamping & sliding' mechanism

The physico-mathematical modeling of 'Clamping & sliding' is based on the following equation for the evolution of the unidimensional density $\rho(x, t)$ of ParB along DNA, fully described in (Walter et al., 2020):

$$\frac{\partial \rho(x,t)}{\partial t} = D\Delta\rho(x,t) + R\delta(x) - U\rho(x,t)$$

where x is the genomic coordinate from *parS*, t the time, D the diffusion coefficient, R the release rate and U the unbinding rate. The symbol Δ (unidimensional Laplacian) stands for the diffusion (improperly called sliding) and δ is the delta function equal to 1 if $x = 0$ and 0 otherwise. It accounts for the release of ParB as a clamp, which occurs exclusively at *parS* (*i.e.*, when $x = 0$).

In the stationary state $\frac{\partial \rho(x,t)}{\partial t} = 0$, the solution $n(x) = \rho(x,t)\epsilon$ corresponding to the coarse-grained density of ParB at the scale of the footprint $\epsilon = 16\ bp$ is:

$$n(x) = A\epsilon e^{-x/\mu}$$

where $A = R/\sqrt{DU}$ is an overall amplitude and $\mu = \sqrt{D/U}$ is the characteristic length of the distribution.

The parameters R, D and U have been previously determined with the values $R = 1.9\ s^{-1}$, $D = 4.3.10^5\ bp^2\ s^{-1}$ (~0.05 $\mu m^2\ s^{-1}$) and $U = 4.7.10\text{-}3\ s^{-1}$ (Walter et al., 2020).

DATA AVAILABILITY STATEMENT

The raw and processed ChIP-seq data reported in this paper have been deposited in GEOdatabase (NCBI) under the accession number GSE256357. Unpublished custom codes are available upon request.

ACKNOWLEDGEMENTS

We thank all members of the GeDy (CBI) and the SCPN (L2C) teams for fruitful discussions. We thank P. Higgins for the LT2 strains. We acknowledge the staff at the GeT-Biopuces platform (INSA, Toulouse) for handling libraries and sequencing of the ChIP-seq samples. This work was supported by the CNRS 80Prime MITI grant (Numacoiled) and the CNRS "Modélisation pour le Vivant" MITI Grant (CoilChrom).

AUTHOR CONTRIBUTIONS

Conceptualization, J.-C.W. and J.-Y.B.;

Data curation, D. L and J.-Y.B.;

Formal analysis, M.C., J.-Y.B., and J.-C.W.;

Funding Acquisition, J.-C.W. and J.-Y.B.;

Investigation, H.S.A., V.Q., D.-D.R., J.R., J.-C.W., and J.-Y.B.;

Methodology, H.S.A., V.Q., J.-C.W. and J.-Y.B.;

Project administration, J.-Y.B.;

Resources, F.C., M.C., J.-Y.B.;

Software, M.C., J.-Y.B.;

Supervision, J.-Y.B.;

Validation, H.S.A., J.R., D. L., J.-C.W., and J.-Y.B.;

Visualization, H.S.A., J.-C.W. and J.-Y.B.;

Writing – original draft, H.S.A., J.-C.W. and J.-Y.B.;

Writing – Review & Editing, M.C., F.C., H.S.A., J.-C.W., and J.-Y.B.

CONFLICT OF INTEREST STATEMENT

The authors declare that they have no conflicts of interest with the contents of this article.

ETHICS STATEMENT

This article does not contain any studies with human or animal subjects.

FIGURES LEGEND

Figure 1: Schematic of ParB dimers and the first steps of the assembly of the partition complex.

A- Open (left) and closed (right) conformations mediated by CTP and *parS* DNA. ParB is a homodimer composed of a C-terminal dimerization domain (orange) link to the central (light blue) and N-terminal (dark blue) domains by a flexible linker (red). The central domain contains the two DNA binding motifs for *parS* binding (Sanchez et al., 2013). The N-terminal part contains the ParA interaction domain, the arginine-like motif, the CTP binding motif and the multimerization domain (Ah-Seng et al., 2009; Soh et al., 2019; Surtees and Funnell, 1999). In the presence of CTP ParB dimer forms a clamp around *parS* DNA. **B-** Schematic representation of the initial steps for the partition complex assembly. The open conformation of ParB dimer (top right) enables DNA binding to the central part of ParB. Upon specific binding to *parS* centromere (step B), ParB undergoes a conformational change (represented as ParB rounded in the N-terminal part) promoting CTP binding, which subsequently induces ParB to form a clamp around *parS* (step C). Clamping promotes ParB release from *parS* and allow the ParB clamp to slide away from *parS* by free diffusion (step S), and to free the *parS* loading site for a next round of loading. After CTP or CDP (upon CTP hydrolysis) unbinding, ParB switches back to an open conformation enabling its unloading from the DNA (step U) hydrolysis. This representation has been updated from (Walter et al., 2020). **C-** Schematic representation of the ParB-ParB long distance interactions. The ParB diffusing along the *parS*-proximal DNA interacts with other ParB dimers, either in the open (left) or close (right) conformations. These interactions may lead to transient bridging leading to DNA condensation (Balaguer et al., 2021; Tisma et al., 2023).

Figure 2: Measurements of DNA supercoiling in various genetic backgrounds.

A- Relative DNA supercoiling level in *E. coli*, LT2 and topoisomerase variants is estimated from the plasmid pSAH01 extracted in growing culture. *E.coli* and LT2 strains were grown at 37°C and 30°C, respectively. 1D agarose gel with 5 $\mu g.ml^{-1}$ chloroquine. **B-** Same as in panel A for LT2 strains resolved in 2D agarose gel with 5 and 8 $\mu g.ml^{-1}$ chloroquine in the first and second dimension (indicated by arrows), respectively. **C-** Measurement of the total supercoiling density in the LT2 *gyrB* strain. DNA of pSAH01, extracted from LT2 *gyrB*, is separated in two aliquots. One was treated by topoI to relax all supercoils, and mix back to the untreated aliquot before separation on a 2D agarose gel, as in B with 1.2 and 8 $\mu g.ml^{-1}$ chloroquine in the first and second dimension, respectively. Mixing both samples allows for a more accurate calculation of the number of supercoils difference (see also Figure S1C). The position of linear DNA (L), resulting from plasmid double-strand breaks during the procedures, are indicated. Note that the top and bottom of the gel are displayed at two different exposures for clarity. Original samples are displayed in Figure S1B. **D-** Summary of the relative supercoiling variations and the calculated total supercoiling density. The relative supercoiling (σ) variations of pSAH01 between each indicated strain were measured from 1D or 2D agarose gels (described in the main text and Figure S1A). The total DNA supercoiling density is calculated from the relaxed form of pSAH01 ($\sigma = 0$) using the relative σ variations between each strain.

Figure 3: ParB DNA binding profiles are highly similar in the two extreme DNA supercoiling densities.

Biological duplicates of ChIP-seq data were performed on *E. coli topA* (blue) and LT2 *gyrB* (red) carrying the F1-10B plasmid. **A-** The ParB reads, normalized to 1 relative to the highest bin, are displayed (ribbon representation) as a function of the genomic coordinates of the plasmid F1-10B, with the line representing the average of the each datasets. Asterisks represent pics that are present only in one replicate of the *topA* dataset (see Figure S2). **B-** Zoom of the data on the right side of *parS*, represented as a function of the genomic distance from *parS*. The correlation coefficients (C) are calculated from coordinates 200 to 10200.

Figure 4: Partition complexes assemble functionally on linear DNA.

A- Schematic of the plasmid F1-10B with the insertions of the *telRL-kan* cassette at several distances (3.5-, 13- and 47-kbp) from *parS*. The open and the blue circles represent the origin of replication (*ori2*) and the centromere site (*parS*), respectively. The dashed blue line represents the variation in distance between *parS* and *telRL* sites. The plasmids F_*telRL* are represented in circular (left) and linear (right) conformations depending on the co-residence of the prophage N15 in the *E. coli* strains (not to scale). **B-** Fluorescence imaging of ParB clusters on circular and linear plasmids *in vivo*. MC1061 *E. coli* cells carrying (bottom panels) or not (top panels) N15 display foci of $ParB_F$-mVenus protein expressed from the endogenous genetic locus on F1-10B and F_*telRL*-mVenus derivatives. Over 99.5% of cells harbor $ParB_F$ foci, except for F_*telRL*3.5 in the presence of N15 displaying ~3% of cells without foci. Scale bars: 2 µm. **C-** Partition function is measured as the percentage of plasmid loss rate from exponentially growing cells per generation. F1-10B, F_*telRL* derivatives and mini-F Δ*parAB*

were introduced in MC1061/N15 cells, resulting in linear conformations for the three F_*telRL* derivatives. Standard deviations derived from three independent measurements. **D-** Positioning of the plasmid F1-10B and its derivatives in MC1061 carrying (+) or not (-) the N15 prophage by fluorescence imaging of ParB-mVenus, performed and displayed in panel B. Statistical analyses of ParB-mVenus foci positioning is performed on cells with one focus (top) or two foci (bottom). The frequency (percent) of cell with foci located in the indicated intervals are plotted or relative to the half (one focus) or the entire (two foci) cell length. Lighter and darker colors correspond the absence or presence of N15 prophage as co-resident with F1-10B (green), F_*telRL*47 (red), F_*telRL*13 (violet) and F_*telRL3.5* (blue) plasmids. The number of cells counted with one focus or two foci were 154 to 527 and 1456 to 3228, respectively.

Figure 5: ParB DNA binding profiles is unaffected by linearization of the plasmid F.

A- Comparison of the ParB DNA binding profiles from ChIP-seq of the circular (wt) and linearized plasmids F1-10B. In the presence of N15, *telRL*47, *telRL*13, *telRL*3.5 are linearized at 47-, 13-, and 3.5-kbp from *parS*, respectively. The ParB density, relative to the highest bin, is plotted against the genomic coordinates with the origin at the last base of the last *parS* site. Note that for F_*telRL*3.5, the profile ends at the telomerisation site (see Figure S5 for profile on both sides of the telomerisation site). **B-** The 'Clamping & sliding' model describes only partly the ParB DNA binding pattern. The ChIP-seq data of the linear F_*telRL*3.5 plasmid (green line), normalize as in panel A, is plotted relative to the coordinate of the highest bin, which is within the centromere site, about 300-bp from the last *parS* repeat. Monte carlo simulations of the 'Clamping & sliding' mechanism have being performed using the same parameters as previously described (Walter et al., 2020), with R, the parameter of ParB release from *parS*, sets as 1.9 or 3 s^{-1} represented by the red and blue lines, respectively. The extremity of the linear DNA at which ParB clamps are able to escape is set at 3800-bp from *parS*.

Figure 6: DNA compaction within partition complexes by ParB-ParB interactions.

A- Schematic model of the ParB-ParB bridging interactions. The model comprises a coarse-grained DNA polymer (depicted as a red line) of length L=658 monomers, each representing 20-bp, corresponding to a total length of ~13-Kbp. ParB proteins (green dots) are distributed according to the ParB DNA binding profile from ChIP-seq assays (see main text). Two close ParB interact with an energy strength *J*. **B-** Dependency of the radius of gyration on ParB-ParB interaction strength. The root mean square (r.m.s.) of the radius of gyration from 600 independent initial ParB distributions is plotted versus *J*. The average curve (blue line) displays a transition between a coil and a globule phase at low and high *J* values, respectively. A drop of ~40% is observed between the two phases, with a critical transition value of J_c ~1.70 +/- 0.1 kT (for details, see Fig. S7B).

REFERENCES

Ah-Seng, Y., Lopez, F., Pasta, F., Lane, D., and Bouet, J.Y. (2009). Dual role of DNA in regulating ATP hydrolysis by the SopA partition protein. J Biol Chem *284*, 30067-30075.

Ah-Seng, Y., Rech, J., Lane, D., and Bouet, J.Y. (2013). Defining the role of ATP hydrolysis in mitotic segregation of bacterial plasmids. PLoS genetics *9*, e1003956.

Azaldegui, C.A., Vecchiarelli, A.G., and Biteen, J.S. (2020). The Emergence of Phase Separation as an Organizing Principle in Bacteria. Biophys J.

Babl, L., Giacomelli, G., Ramm, B., Gelmroth, A.K., Bramkamp, M., and Schwille, P. (2022). CTP-controlled liquid-liquid phase separation of ParB. J Mol Biol *434*, 167401.

Balaguer, F.A., Aicart-Ramos, C., Fisher, G.L., de Braganca, S., Martin-Cuevas, E.M., Pastrana, C.L., Dillingham, M.S., and Moreno-Herrero, F. (2021). CTP promotes efficient ParB-dependent DNA condensation by facilitating one-dimensional diffusion from parS. eLife *10*.

Biek, D.P., and Shi, J.P. (1994). A single 43-bp sopC repeat of plasmid mini-F is sufficient to allow assembly of a functional nucleoprotein partition complex. Proc Natl Acad Sci USA *91*, 8027-8031.

Bouet, J.Y., Bouvier, M., and Lane, D. (2006). Concerted action of plasmid maintenance functions: partition complexes create a requirement for dimer resolution. Mol Microbiol *62*, 1447-1459.

Bouet, J.Y., and Funnell, B.E. (2019). Plasmid Localization and Partition in Enterobacteriaceae. EcoSal Plus *8*, ESP-0003-2019.

Bouet, J.Y., and Lane, D. (2009). Molecular basis of the supercoil deficit induced by the mini-F plasmid partition complex. J Biol Chem *284*, 165-173.

Bowman, G.R., Comolli, L.R., Zhu, J., Eckart, M., Koenig, M., Downing, K.H., Moerner, W.E., Earnest, T., and Shapiro, L. (2008). A polymeric protein anchors the chromosomal origin/ParB complex at a bacterial cell pole. Cell *134*, 945-955.

Champion, K., and Higgins, N.P. (2007). Growth rate toxicity phenotypes and homeostatic supercoil control differentiate Escherichia coli from Salmonella enterica serovar Typhimurium. J Bacteriol *189*, 5839-5849.

Conter, A., Menchon, C., and Gutierrez, C. (1997). Role of DNA supercoiling and rpoS sigma factor in the osmotic and growth phase-dependent induction of the gene osmE of Escherichia coli K12. J Mol Biol *273*, 75-83.

Cornet, F., Blanchais, C., Dusfour-Castan, R., Meunier, A., Quebre, V., Sekkouri Alaoui, H., Boudsoq, F., Campos, M., Crozat, E., Guynet, C., *et al.* (2023). DNA Segregation in Enterobacteria. EcoSal Plus, eesp00382020.

Cui, T., Moro-oka, N., Ohsumi, K., Kodama, K., Ohshima, T., Ogasawara, N., Mori, H., Wanner, B., Niki, H., and Horiuchi, T. (2007). Escherichia coli with a linear genome. EMBO Rep *8*, 181-187.

Debaugny, R.E., Sanchez, A., Rech, J., Labourdette, D., Dorignac, J., Geniet, F., Palmeri, J., Parmeggiani, A., Boudsocq, F., Anton Leberre, V., *et al.* (2018). A conserved mechanism drives partition complex assembly on bacterial chromosomes and plasmids. Mol Syst Biol *14*, e8516.

Diaz, R., Rech, J., and Bouet, J.Y. (2015). Imaging centromere-based incompatibilities: Insights into the mechanism of incompatibility mediated by low-copy number plasmids. Plasmid *80*, 54-62.

Diaz, R.E., Sanchez, A., Anton Le Berre, V., and Bouet, J.Y. (2017). High-Resolution Chromatin Immunoprecipitation: ChIP-Sequencing. Methods in molecular biology (Clifton, NJ *1624*, 61-73.

Goldstein, E., and Drlica, K. (1984). Regulation of bacterial DNA supercoiling: plasmid linking numbers vary with growth temperature. Proc Natl Acad Sci U S A *81*, 4046-4050.

Gordon, G.S., Sitnikov, D., Webb, C.D., Teleman, A., Straight, A., Losick, R., Murray, A.W., and Wright, A. (1997). Chromosome and low copy plasmid segregation in *E. coli*: Visual evidence for distinct mechanisms. Cell *90*, 1113-1121.

Guilhas, B., Walter, J.C., Rech, J., David, G., Walliser, N.O., Palmeri, J., Mathieu-Demaziere, C., Parmeggiani, A., Bouet, J.Y., Le Gall, A., *et al.* (2020). ATP-Driven Separation of Liquid Phase Condensates in Bacteria. Mol Cell *79*, 293-303 e294.

Harms, A., Treuner-Lange, A., Schumacher, D., and Sogaard-Andersen, L. (2013). Tracking of Chromosome and Replisome Dynamics in Myxococcus xanthus Reveals a Novel Chromosome Arrangement. PLoS genetics *9*, e1003802.

Jalal, A.S., Tran, N.T., and Le, T.B. (2020). ParB spreading on DNA requires cytidine triphosphate in vitro. eLife *9*, e53515.

Jalal, A.S., Tran, N.T., Stevenson, C.E., Chimthanawala, A., Badrinarayanan, A., Lawson, D.M., and Le, T.B. (2021). A CTP-dependent gating mechanism enables ParB spreading on DNA. eLife *10*.

Jalal, A.S.B., and Le, T.B.K. (2020). Bacterial chromosome segregation by the ParABS system. Open biology *10*, 200097.

Junier, I., Ghobadpour, E., Espeli, O., and Everaers, R. (2023). DNA supercoiling in bacteria: state of play and challenges from a viewpoint of physics based modeling. Frontiers in microbiology *14*, 1192831.

Lin, D.C.H., and Grossman, A.D. (1998). Identification and characterization of a bacterial chromosome partitioning site. Cell *92*, 675-685.

Livny, J., Yamaichi, Y., and Waldor, M.K. (2007). Distribution of centromere-like parS sites in bacteria: insights from comparative genomics. J Bacteriol *189*, 8693-8703.

Newman, M.E.J., and Barkema, G.T. (1999). Monte Carlo methods in statistical physics. Clarendon Press, Oxford.

Niki, H., and Hiraga, S. (1997). Subcellular distribution of actively partitioning F plasmid during the cell division cycle in *E. coli*. Cell *90*, 951-957.

Ogura, T., Niki, H., Mori, H., Morita, M., Hasegawa, M., Ichinose, C., and Hiraga, S. (1990). Identification and characterization of gyrB mutants of Escherichia coli that are defective in partitioning of mini-F plasmids. J Bacteriol *172*, 1562-1568.

Osorio-Valeriano, M., Altegoer, F., Das, C.K., Steinchen, W., Panis, G., Connolley, L., Giacomelli, G., Feddersen, H., Corrales-Guerrero, L., Giammarinaro, P.I., *et al.* (2021). The CTPase activity of ParB determines the size and dynamics of prokaryotic DNA partition complexes. Mol Cell *81*, 3992-4007 e3910.

Osorio-Valeriano, M., Altegoer, F., Steinchen, W., Urban, S., Liu, Y., Bange, G., and Thanbichler, M. (2019). ParB-type DNA Segregation Proteins Are CTP-Dependent Molecular Switches. Cell *179*, 1512-1524 e1515.

Pettijohn, D.E., and Pfenninger, O. (1980). Supercoils in prokaryotic DNA restrained in vivo. Proc Natl Acad Sci U S A *77*, 1331-1335.

Pillet, F., Sanchez, A., Lane, D., Anton Leberre, V., and Bouet, J.Y. (2011). Centromere binding specificity in assembly of the F plasmid partition complex. Nucleic Acids Res *39*, 7477-7486.

Ravin, N.V. (2003). Mechanisms of replication and telomere resolution of the linear plasmid prophage N15. FEMS Microbiol Lett *221*, 1-6.

Rodionov, O., Lobocka, M., and Yarmolinsky, M. (1999). Silencing of genes flanking the P1 plasmid centromere. Science *283*, 546-549.

Rovinskiy, N.S., Agbleke, A.A., Chesnokova, O.N., and Higgins, N.P. (2019). Supercoil Levels in E. coli and Salmonella Chromosomes Are Regulated by the C-Terminal 35(-)38 Amino Acids of GyrA. Microorganisms *7*.

Sanchez, A., Cattoni, D.I., Walter, J.C., Rech, J., Parmeggiani, A., Nollmann, M., and Bouet, J.Y. (2015). Stochastic Self-Assembly of ParB Proteins Builds the Bacterial DNA Segregation Apparatus. Cell Syst *1*, 163-173.

Sanchez, A., Rech, J., Gasc, C., and Bouet, J.Y. (2013). Insight into centromere-binding properties of ParB proteins: a secondary binding motif is essential for bacterial genome maintenance. Nucleic Acids Res *41*, 3094-3103.

Soh, Y.M., Davidson, I.F., Zamuner, S., Basquin, J., Bock, F.P., Taschner, M., Veening, J.W., De Los Rios, P., Peters, J.M., and Gruber, S. (2019). Self-organization of parS centromeres by the ParB CTP hydrolase. Science *366*, 1129-1133.

Surtees, J.A., and Funnell, B.E. (1999). P1 ParB domain structure includes two independent multimerization domains. J Bacteriol *181*, 5898-5908.

Tisma, M., Janissen, R., Antar, H., Martin-Gonzalez, A., Barth, R., Beekman, T., van der Torre, J., Michieletto, D., Gruber, S., and Dekker, C. (2023). Dynamic ParB-DNA interactions initiate and maintain a partition condensate for bacterial chromosome segregation. Nucleic Acids Res *51*, 11856-11875.

Tisma, M., Panoukidou, M., Antar, H., Soh, Y.M., Barth, R., Pradhan, B., Barth, A., van der Torre, J., Michieletto, D., Gruber, S., *et al.* (2022). ParB proteins can bypass DNA-bound roadblocks via dimer-dimer recruitment. Science advances *8*, eabn3299.

van der Valk, R.A., Vreede, J., Cremazy, F., and Dame, R.T. (2014). Genomic looping: a key principle of chromatin organization. Journal of molecular microbiology and biotechnology *24*, 344-359.

Vanderzande, C. (1998). Lattice Models of Polymers. Cambridge University Press, Cambridge.

Walter, J.C., Lepage, T., Dorignac, J., Geniet, F., Parmeggiani, A., Palmeri, J., Bouet, J.Y., and Junier, I. (2021). Supercoiled DNA and non-equilibrium formation of protein complexes: A quantitative model of the nucleoprotein ParBS partition complex. PLoS Comput Biol *17*, e1008869.

Walter, J.C., Rech, J., Walliser, N.O., Dorignac, J., Geniet, F., Palmeri, J., Parmeggiani, A., and Bouet, J.Y. (2020). Physical Modeling of a Sliding Clamp Mechanism for the Spreading of ParB at Short Genomic Distance from Bacterial Centromere Sites. iScience *23*, 101861.

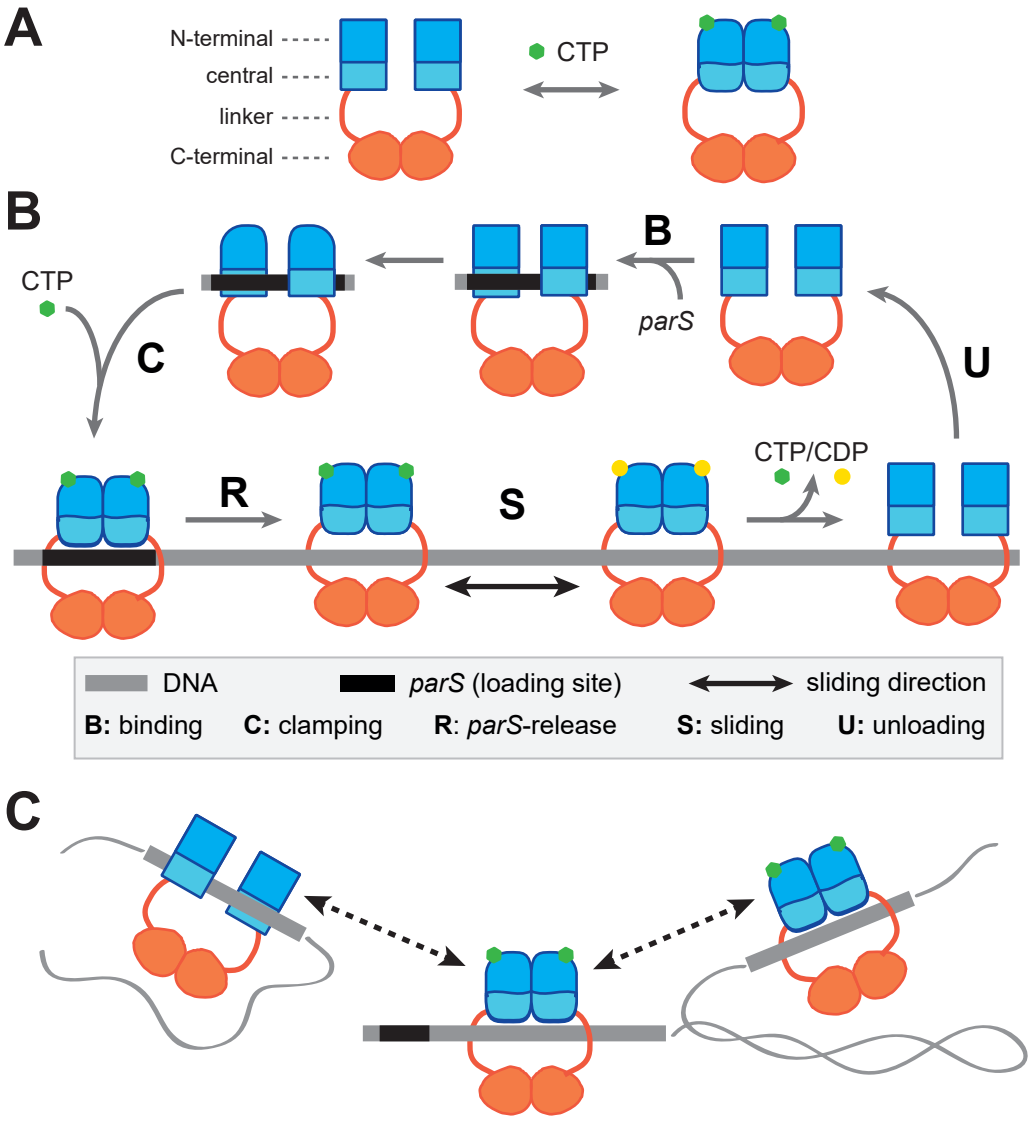
A
N-terminal
central
linker
C-terminal
CTP
B
CTP
C
B
parS
U
CTP/CDP
R
S
DNA
parS (loading site)
sliding direction
B: binding
C: clamping
R: parS-release
S: sliding
U: unloading
C

Figure 1

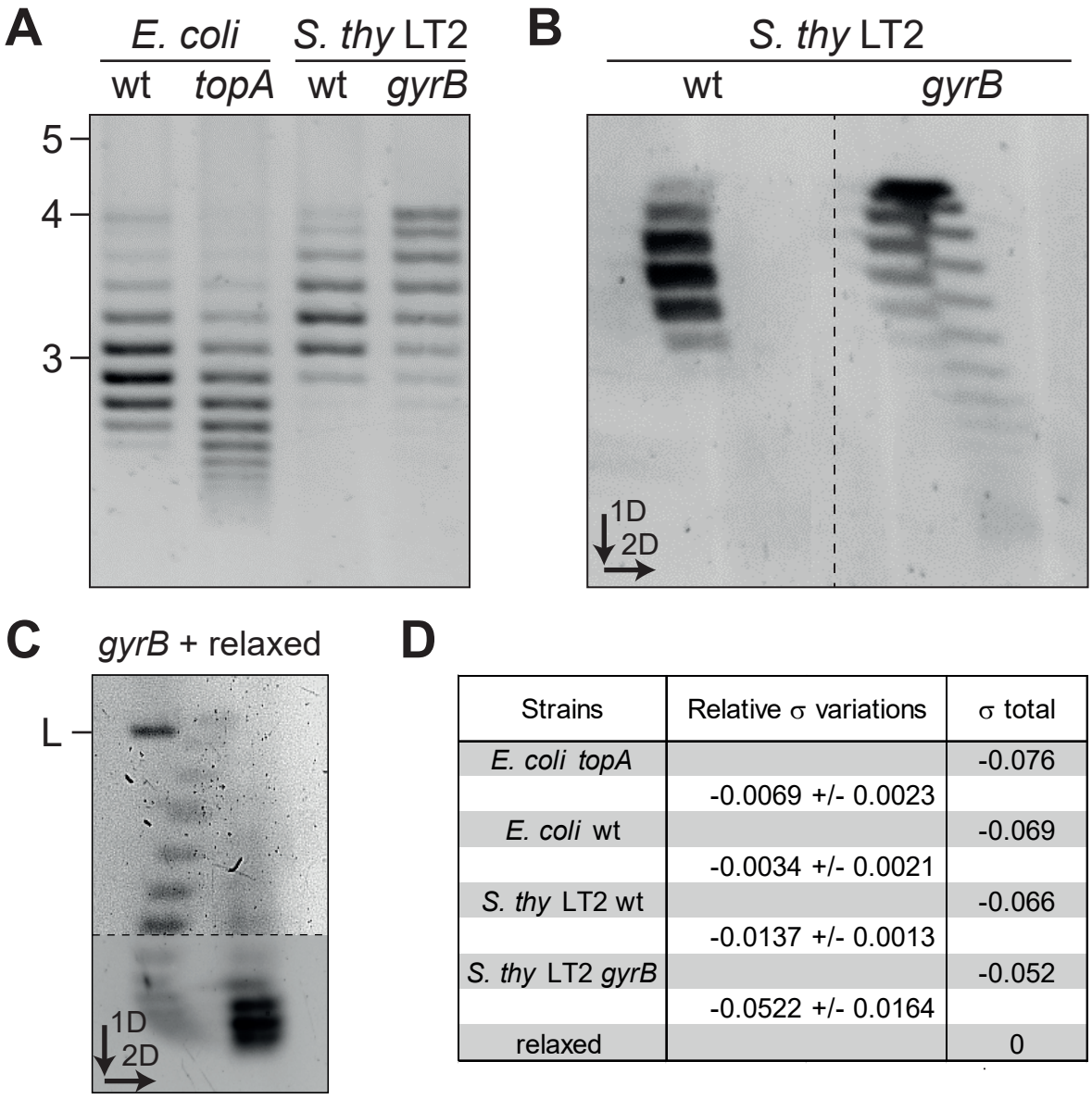

D

Strains	Relative σ variations	σ total
E. coli topA		-0.076
	-0.0069 +/- 0.0023	
E. coli wt		-0.069
	-0.0034 +/- 0.0021	
S. thy LT2 wt		-0.066
	-0.0137 +/- 0.0013	
S. thy LT2 *gyrB*		-0.052
	-0.0522 +/- 0.0164	
relaxed		0

Figure 2

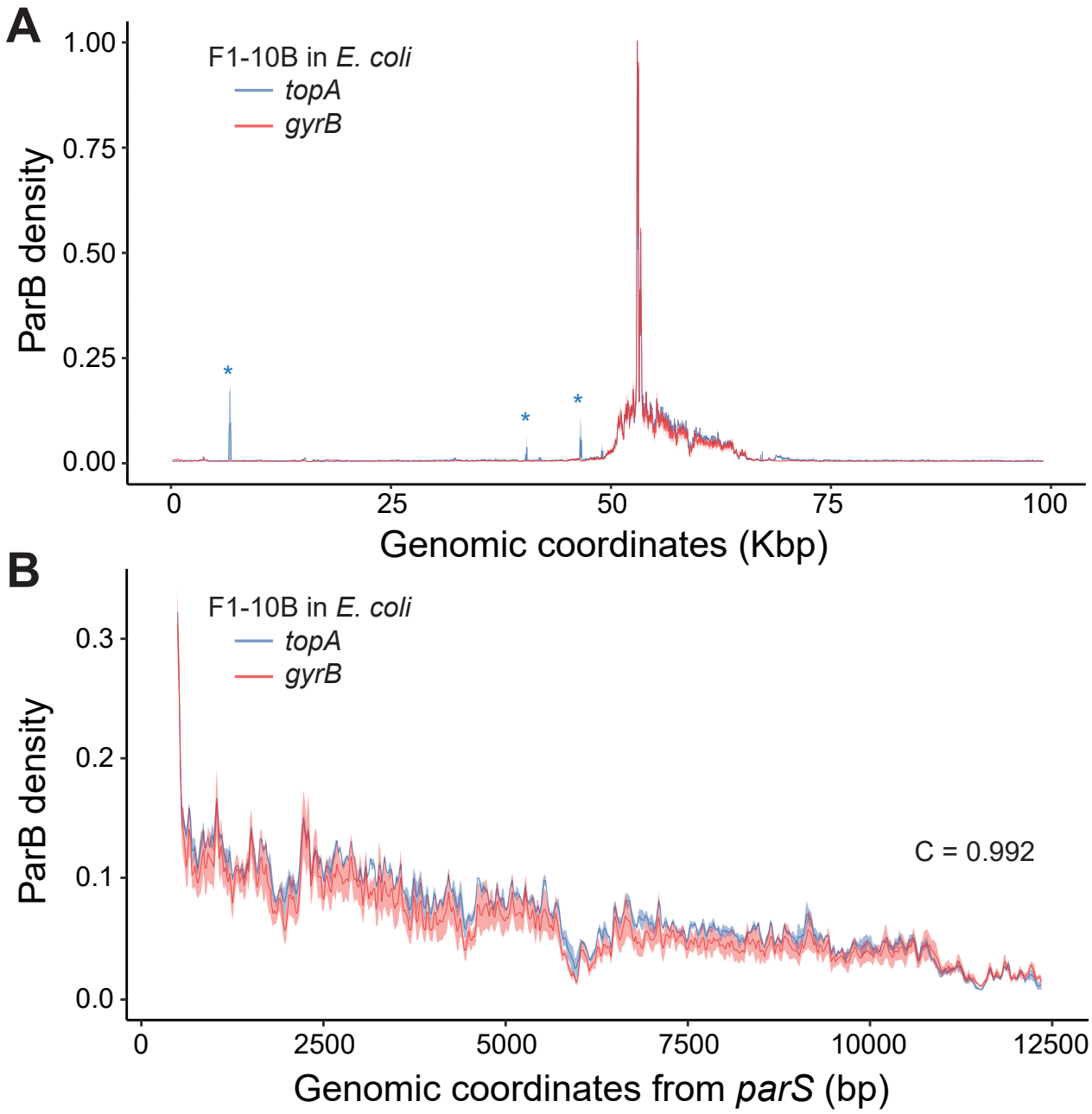
A
F1-10B in E. coli
topA
gyrB
ParB density
1.00
0.75
0.50
0.25
0.00
0
25
50
75
100
Genomic coordinates (Kbp)
B
F1-10B in E. coli
topA
gyrB
ParB density
0.3
0.2
0.1
0.0
C = 0.992
0
2500
5000
7500
10000
12500
Genomic coordinates from parS (bp)

Figure 3

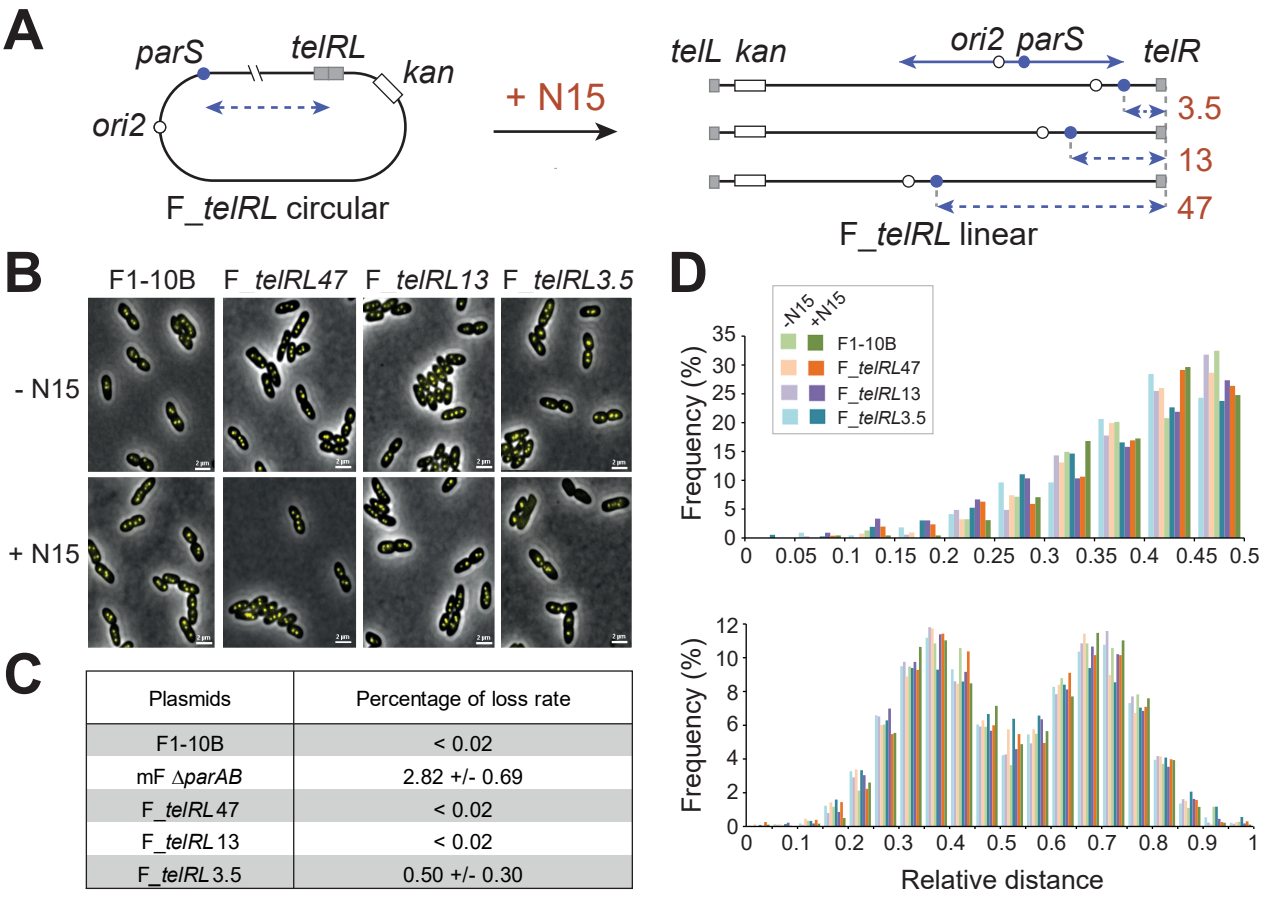

C

Plasmids	Percentage of loss rate
F1-10B	< 0.02
mF Δ*parAB*	2.82 +/- 0.69
F_*telRL* 47	< 0.02
F_*telRL* 13	< 0.02
F_*telRL* 3.5	0.50 +/- 0.30

Figure 4

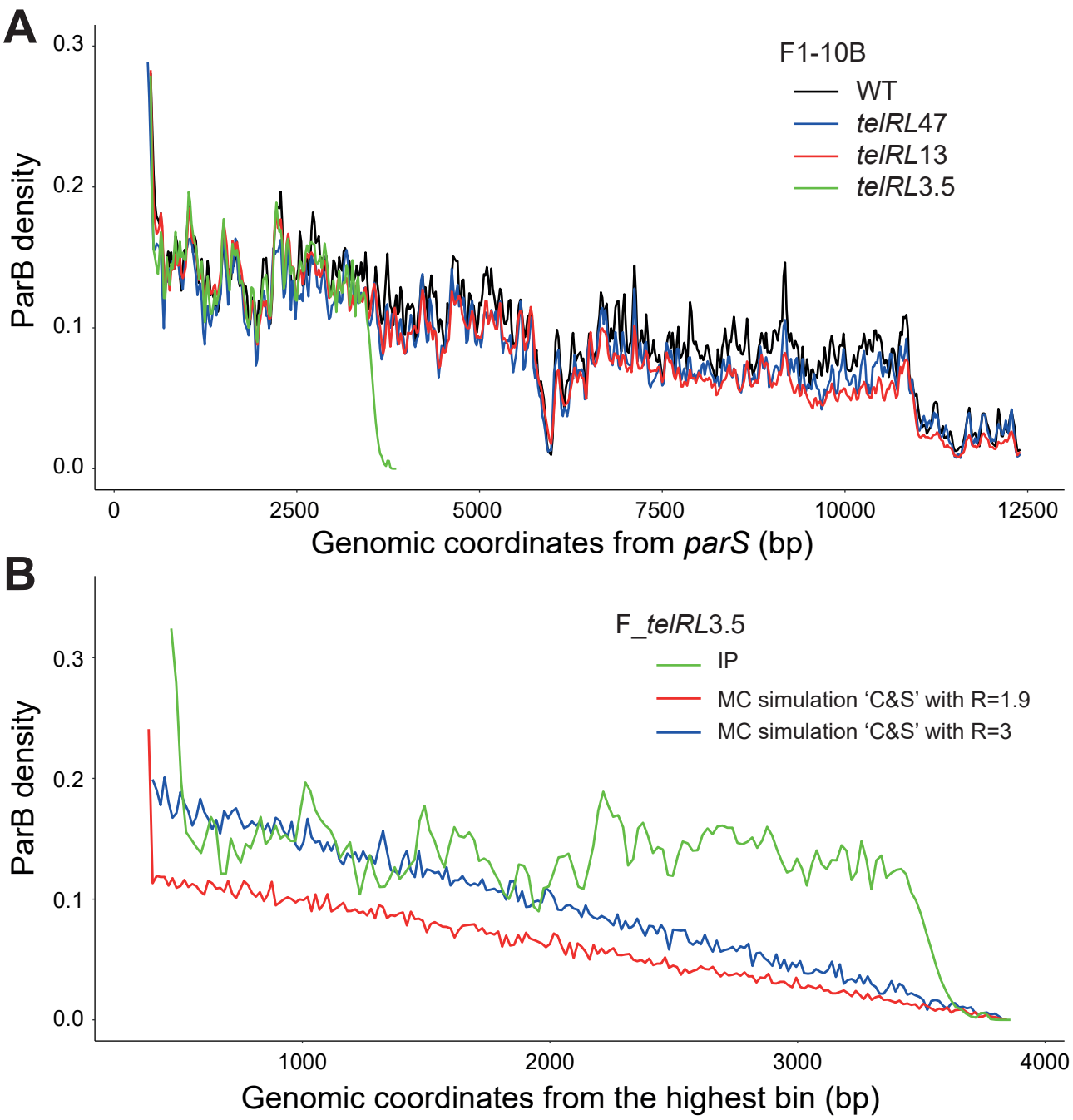
A
F1-10B
WT
telRL47
telRL13
telRL3.5
ParB density
0.3
0.2
0.1
0.0
0
2500
5000
7500
10000
12500
Genomic coordinates from parS (bp)
B
F_telRL3.5
IP
MC simulation 'C&S' with R=1.9
MC simulation 'C&S' with R=3
ParB density
0.3
0.2
0.1
0.0
1000
2000
3000
4000
Genomic coordinates from the highest bin (bp)

Figure 5

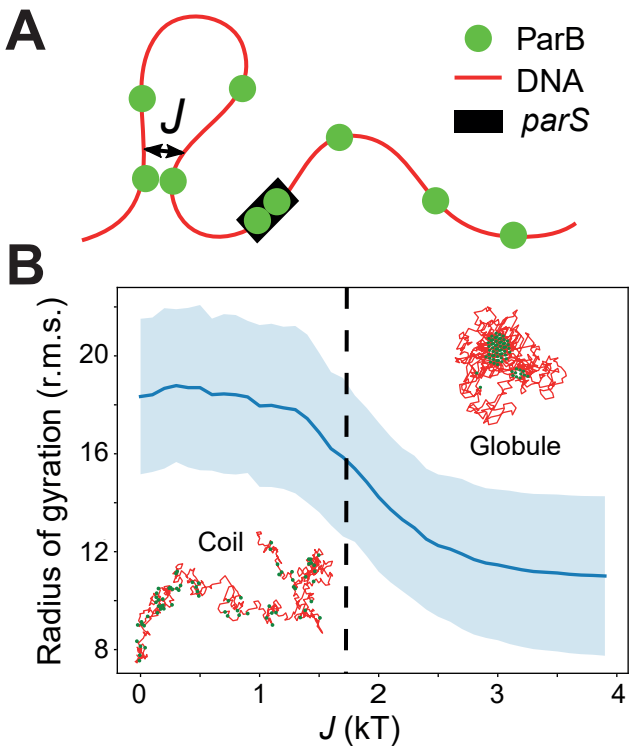
A
ParB
DNA
parS
J
B
Radius of gyration (r.m.s.)
20
16
12
8
Globule
Coil
0
1
2
3
4
J (kT)

Figure 6